JACS
JOURNAL OF THE AMERICAN CHEMICAL SOCIETY

Article

Cite This: *J. Am. Chem. Soc.* 2018, 140, 14870−14877

pubs.acs.org/JACS

Changes in Catalytic and Adsorptive Properties of 2 nm Pt_3Mn Nanoparticles by Subsurface Atoms

Zhenwei Wu,[†] Brandon C. Bukowski,[†] Zhe Li,[‡] Cory Milligan,[†] Lin Zhou,[§] Tao Ma,[§] Yue Wu,[‡] Yang Ren,[∥] Fabio H. Ribeiro,[†] W. Nicholas Delgass,[†] Jeffrey Greeley,[†] Guanghui Zhang,[*,†] and Jeffrey T. Miller[*,†]

[†]Davidson School of Chemical Engineering, Purdue University, West Lafayette 47907, Indiana, United States
[‡]Department of Chemical and Biological Engineering, Iowa State University, Ames 50011, Iowa, United States
[§]Department of Materials Science, Ames Laboratory, Ames 50012, Iowa, United States
[∥]X-Ray Science Division, Argonne National Laboratory, Argonne 60439, Illinois, United States

Supporting Information

ABSTRACT: Supported multimetallic nanoparticles (NPs) are widely used in industrial catalytic processes, where the relation between surface structure and function is well-known. However, the effect of subsurface layers on such catalysts remains mostly unstudied. Here, we demonstrate a clear subsurface effect on supported 2 nm core−shell NPs with atomically precise and high temperature stable Pt_3Mn intermetallic surface measured by *in situ* synchrotron X-ray Diffraction, difference X-ray Absorption Spectroscopy, and Energy Dispersive X-ray Spectroscopy. The NPs with a Pt_3Mn subsurface have 98% selectivity to C−H over C−C bond activation during propane dehydrogenation at 550 °C compared with 82% for core−shell NPs with a Pt subsurface. The difference is correlated with significant reduction in the heats of reactant adsorption due to the Pt_3Mn intermetallic subsurface as discerned by theory as well as experiment. The findings of this work highlight the importance of subsurface for supported NP catalysts, which can be tuned via controlled intermetallic formation. Such approach is generally applicable to modifying multimetallic NPs, adding another dimension to the tunability of their catalytic performance.

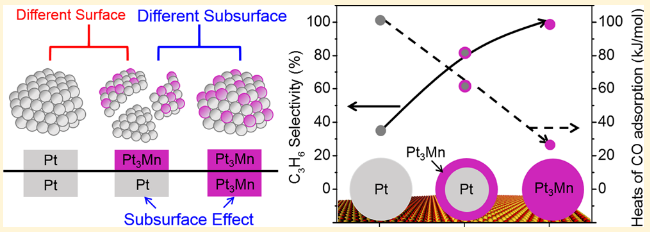

INTRODUCTION

Supported multimetallic nanoparticles (NPs) are among the most widely used catalysts in industry, and their properties are highly tunable by control of their composition and structure.[1,2] The geometric and electronic effects related to the NP surface have been well studied since the early work of Sinfelt.[3] It has been, however, very difficult to identify any subsurface effects on NPs, even while changing the subsurface metal atoms has been observed to have a large impact on single crystal model catalysts by surface science and Density Functional Theory (DFT) studies,[4−7] as well as recently in electrochemical processes.[7−9]

For supported NPs, the challenges to study the effect of subsurface layers lie in the difficulties in preparing and characterizing materials with the same surface structure but different subsurface phases. It was previously suggested that substituting a Pt NP core with a second noble metal improved its activity for preferential oxidation of carbon monoxide in hydrogen below 200 °C.[10,11] Nevertheless, the structure of such catalyst was not determined under reaction condition, and it was not stable at higher temperatures due to diffusion between the surface and subsurface, forming a solid solution. This type of phase has randomly disordered bimetallic surface as well as subsurface as typical for noble metal mixtures.[10,12] Further identification and investigation of the subsurface effect on supported NPs require improved methods to separately control and characterize surfaces and subsurfaces that are atomically precise and high temperature stable.

More stable NP core−shell structures can be achieved by intermetallic compound phases which feature precisely ordered arrays of different metals.[13,14] They contain strong heteroatomic bonds that minimize atomic diffusion and structural changes.[15,16] NPs with intermetallic shells on top of a heterogeneous core have been recently shown to maintain surface ordering at high temperatures.[17] Herein, we investigate the effect of subsurface composition on supported 2 nm core−shell NPs (Pt_3Mn shell on Pt core) versus full-body intermetallic NPs (Pt_3Mn shell on Pt_3Mn core). A Pt_3Mn subsurface instead of Pt significantly improves the catalytic selectivity for C−H activation for propane dehydrogenation at 550 °C, which is correlated to a large decrease of adsorbate binding strength according to DFT calculation as well as experimental measurements. The subsurface effect offers enhanced catalytic performance and tunable adsorptive

Received: August 20, 2018
Published: October 15, 2018

DOI: 10.1021/jacs.8b08162
J. Am. Chem. Soc. 2018, 140, 14870−14877

properties, demonstrating its potential in modifying NP catalysts for many reactions.

EXPERIMENTAL SECTION

Catalyst Synthesis. Two Pt−Mn/SiO_2 catalysts, namely Pt_3Mn and Pt_3Mn-s, were synthesized by sequential incipient wetness impregnation (IWI). The pH of the impregnated solutions was controlled to be around 11, guided by the strong electrostatic adsorption (SEA) method, which ensured uniform nanoparticle sizes. To prepare Pt_3Mn, 2.28 g of manganese nitrate tetrahydrate (Sigma-Aldrich) and 3.49 g of citric acid (Sigma-Aldrich) were dissolved in 3.0 mL of deionized water. The pH of the solution was adjusted by adding 30% ammonium hydroxide solution (Sigma-Aldrich), and the volume was adjusted to 7.5 mL by adding deionized water. This manganese precursor solution was then added dropwise to 10.0 g of silica (Davisil 636 silica gel from Sigma−Aldrich, 480 m^2/g and 0.75 mL/g pore volume) and stirred. The resulting solids were dried overnight at 125 °C and calcined at 550 °C for 3 h. On the obtained Mn/SiO_2, a second impregnation was conducted to load platinum. 0.20 g of tetraammineplatinum nitrate (Sigma−Aldrich) was dissolved in 3.0 mL of deionized water, whose pH was again adjusted to 11 by 30% ammonium hydroxide solution. The resulting solution was added dropwise to 5.0 g of Mn/SiO_2, and the resulting material was dried overnight at 125 °C, calcined at 225 °C for 3 h, and further reduced at 550 °C in 5% H_2/N_2 at 50 cm^3/min for 0.5 h. The same procedure was used to prepare the Pt_3Mn-s catalyst, except that in the first step, 0.91 g of manganese nitrate tetrahydrate and 1.40 g of citric acid were used to prepare the manganese precursor solution. Also prepared was a monometallic Pt/SiO_2 catalyst with 2 wt % Pt, on which platinum was loaded by the same procedure as the second impregnation step in the preparation of Pt−Mn catalysts.

Characterization of Supported 2 nm NPs. Scanning transmission electron microscopy (STEM) images were taken at Birck Nanotechnology Center at Purdue University using an FEI Titan Scanning Transmission Electron Microscope (80−300 kV, 1 nm spatial resolution in STEM). Energy-Dispersive X-ray Spectroscopy was measured on a Titan Themis 300 probe corrected TEM with a Super-X EDX detector from Sensitive Instrument Facility of Ames Laboratory. *In situ* synchrotron X-ray diffraction (sXRD) measurements were performed at the 11-ID-C insertion device beamline at the advanced photon source (APS), Argonne National Laboratory. Data were acquired in Laue transmission mode using X-rays at 105.59 keV (λ = 0.117418 Å) and a PerkinElmer large area detector with typical exposure times of 5 s, a total of 30 exposures and 3 scans for each sample. Samples were pressed into a thin pellet and loaded into a Linkam Thermal Stage which allowed reactant gas flow during the *in situ* measurements. *In situ* X-ray absorption spectroscopy (XAS) at the Pt L_{III} edge (11.564 keV) and Mn K edge (6.539 keV) were taken on the 10-BM bending magnet beamline of the Materials Research Collaborative Access Team (MRCAT) at the Advanced Photon Source (APS), Argonne National Laboratory. The data were collected in transmission mode. Catalyst samples as well as reference compounds were ground into fine powders and pressed into a cylindrical sample holder, which was loaded into a tube reactor allowing gas flow during *in situ* measurement. X-ray photoelectron spectroscopy (XPS) data were obtained using a Kratos Axis Ultra DLD spectrometer with monochromic Al Kα radiation (1486.6 eV) at pass energy of 20 and 160 eV for high-resolution and survey spectra, respectively. A commercial Kratos charge neutralizer was used to avoid nonhomogeneous electric charge of nonconducting powder and to achieve better resolution. The XPS data were collected on reduced samples after they were transferred in vacuum to the spectrometer sample stage and were not exposed to air.

Propane Dehydrogenation. Evaluation of the propane dehydrogenation performance was carried out in a quartz fixed-bed reactor with 3/8-in. (~1 cm) inner diameter. The catalysts with weights ranging from 10 mg to 100 mg were diluted with SiO_2 to achieve total bed weight of 1 g and height of ~3 cm. A thermocouple within a stainless steel thermocouple well was placed at the center of the catalyst bed to measure the reaction temperature inside the bed. The products were analyzed with an Agilent 7890A gas chromatograph system equipped with a Flame Ionization Detector (FID). Before each test at 550 °C, the catalyst was first reduced under 50 cm^3/min 5% H_2/N_2, while the temperature was raised to 550 °C at a rate of 15 °C/min and held at 550 °C for 30 min. For all propane dehydrogenation measurements, the reaction atmosphere contained 1.25% C_3H_8 and varied concentration of H_2 balanced in N_2 with a total flow rate of 200 cm^3/min.

CO Equilibrium Chemisorption. The CO chemisorption uptakes were measured at various temperatures from −115 to 500 °C on a Micromeritics Autochem 2920 automated catalyst characterization system. Around 0.1 g of the catalyst was loaded into a U-shaped quartz reactor tube. Before each chemisorption experiment, the catalyst was first heated to 550 °C at 20 °C/min in 50 cm^3/min of 5% H_2/N_2, kept at this temperature for 0.5 h, and then cooled to 350 °C in the same atmosphere before the flow was switched to 50 cm^3/min of He. After purging with He at 350 °C for 0.5 h, the catalyst was further cooled or heated to the temperature where the CO pulses were dosed and the measurements were taken. CO coverages at different temperatures $\theta(T)$ were calculated by normalizing the corresponding CO uptakes to the saturated CO adsorption.

Density Functional Theory. All DFT calculations are performed with self-consistent, periodic, density function theory using the Vienna Ab-initio Simulation Package (VASP).[18−21] The Perdew−Burke−Ernzerhof (PBE) exchange-correlation function[22] using projector augmented wave (PAW) pseudopotentials was used.[23,24] All calculations are performed with spin polarization. For bulk lattices of Pt and Pt_3Mn a cutoff energy of 600 eV was considered with a force-convergence criterion of 20 meV/Å. The Methfessel-Paxton smearing method was used with a Gamma-centered 10 × 10 × 10 K-point grid. Relaxed lattice constants for bulk Pt and Pt_3Mn were found to be a = 3.98 Å and a = 3.93 Å, respectively. 2 × 2 × 5 surface slabs of the (111) surface were cut for both Pt and Pt_3Mn and included 10 Å of vacuum above the surface. A dipole correction was applied parallel to the plane of the slab to reduce image−image interaction errors. The bottom two layers of the slab were constrained to their bulk lattice positions, while the top three layers were allowed to relax. A cutoff energy of 450 eV was used for all slab calculations with a Gamma-centered 7 × 7 × 1 K-point grid with a similar force-convergence criterion of 20 meV/ Å. High index (211) surfaces were cut from the same bulk to have 4 terrace layers and a step length of 4 platinum atoms. A 4 × 4 × 1 Gamma-centered K-point grid was used for the high index surfaces. Adsorption of all adsorbates was considered at all symmetrically distinct (111) sites corresponding to a 0.25 ML coverage. For gas-phase adsorbate calculations, the same cutoff energy was used with Gaussian smearing of the Fermi energy in an oblong simulation box with dimensions 12 × 13 × 14 Å. For calculations with a Pt_3Mn skin, a single Mn atom replaced Pt in the pure Pt(111) surface and then relaxed at the fixed pure Pt lattice constant. A similar process is used for films containing two layers of Pt_3Mn. For high index (211) surfaces, CO was adsorbed along the step edges. Pt d-band centers were calculated as the first moment of the projected d-electron density of states of surface platinum atoms. The maximum allowed energy was 5 eV above the Fermi edge, consistent for all alloys. Projected density of states was calculated at the same computational parameters as reported for adsorption, with the exceptions being the use of tetrahedral smearing and a denser K-point grid of 15 × 15 × 1.

RESULTS AND DISCUSSION

2 nm Supported Intermetallic NPs with the Same Surface Structure but Different Subsurface. To obtain stable NPs with varying subsurface structures, catalyst synthesis was conducted through diffusion-controlled intermetallic compound formation between catalytic metal platinum and non-noble metal promoter manganese. The metal precursors were loaded on SiO_2 support sequentially and first reduced at 200 °C where monometallic Pt NPs formed. At higher temperature, Mn started to be reduced by hydrogen spilled over from the surface of Pt NPs. The reduced Mn diffused onto the Pt surface and then into the Pt lattice in a kinetically limited fashion, as has been observed for many other bimetallic catalysts prepared in similar way.[25−29] Transformation from Pt to Pt_3Mn intermetallic compounds occurred starting from the surface of the NPs. Manipulating the amount of Mn precursor resulted in partial or full intermetallic transformation, forming core−shell or full-body intermetallic NPs (named as Pt_3Mn-s (s stands for surface) and Pt_3Mn, respectively). The size of the intermetallic NPs depended on that of the parent Pt NPs, which was controlled during impregnation by anchoring of the positively charged metal precursors to the deprotonated surface hydroxyl groups on the support under controlled pH.[30] The two Pt- Mn catalysts have almost identical sizes (~2.0 ± 0.5 nm) according to Scanning Transmission Electron Microscope (STEM) images (Figure S1). A reference Pt catalyst with a similar size was prepared by the same procedure.

To verify intermetallic formation to different extents, the crystal order of the catalysts was first characterized by diffraction (Figure 1). Though diffraction is often considered as a standard technique, it is generally not possible for supported 2 nm NPs using either laboratory X-ray sources or an electron microscope. We turned to *in situ* synchrotron XRD (λ = 0.117418 Å) in Laue transmission configuration, which provides excellent signal-to-noise ratio and resolution for observing the very low intensity NP diffraction, even including the very small superlattice features. Background subtracted NP diffraction signals are shown in Figure 1a. All three catalysts have broad peaks corresponding to 2 nm NPs. No features related to pure Mn metal are observed. Compared to the reference Pt catalyst, the two Pt−Mn catalysts both show diffraction peaks at slightly higher 2 thetas (Figure 1b), indicating smaller average lattice constants (Table S1) and incorporation of Mn atoms. The pattern of the Pt_3Mn catalyst (blue) matches well with the standard of Pt_3Mn intermetallic compound (purple).[31] Weak superlattice diffraction from the (210), (320), and (321) planes (Figure 1b) characteristic of $L1_2$ ordering in Pt_3Mn is also observed, diagnostic of Pt_3Mn intermetallic compound (Figure 1c) forming on this catalyst. The pattern of the Pt_3Mn-s catalyst (red) also shows superlattice diffraction from $L1_2$ symmetry. Its major diffraction peaks, however, are between those of Pt and Pt_3Mn (Figure 1b), suggesting that it contains both Pt and Pt_3Mn phases. The peaks are broader (Table S1) compared to the other two samples despite their similar sizes, which implies larger microstrain characteristic of a coherent two-phase lattice, as expected for core−shell structures.[8,9,11] We note, in passing, that this microstrain is not sufficiently large to impact the catalytic properties of the particles, as discussed in the SI.

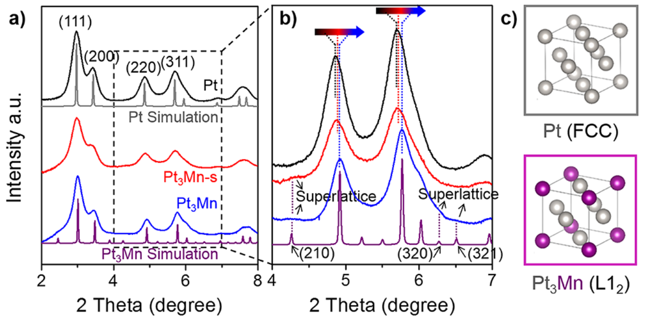

Figure 1. a) Background subtracted *in situ* synchrotron XRD pattern of Pt, Pt_3Mn-s, and Pt_3Mn compared with the simulated pattern of bulk Pt and Pt_3Mn intermetallic phase; b) expanded view of the XRD pattern in the region of 4° to 7°, with color indicators of the peak shifts and superlattice diffraction peaks from the $L1_2$ symmetry in Pt_3Mn intermetallics; c) the unit cell of face centered cubic (fcc) Pt and $L1_2$ type Pt_3Mn intermetallics.

Formation of a partial and full-body Pt_3Mn phase was also inferred from *in situ* XAS. Comparing the reduced Pt−Mn catalysts to Pt NPs, Pt L_{III} edge X-ray Absorption Near Edge Structure (XANES, Figure 2a) shows a slight increase of edge energy and a decrease of whiteline due to incorporation of Mn. The changes are larger for Pt_3Mn compared to Pt_3Mn-s, consistent with the higher Mn content in the former sample. With increasing Mn content, the Pt L_{III} edge Extended X-ray Absorption Fine Structure (EXAFS) spectra (Figure 2b) record decreasing Pt−Pt scattering intensity. Quantitative fitting results (Figure S2, Table S2) are consistent with Pt_3Mn NPs for the Pt_3Mn catalyst (6.3 Pt−Pt at 2.70 Å and 2.8 Pt−Mn at 2.69 Å), as the ratio of the Pt−Pt coordination number to Pt−Mn is around 2, the same as that of the ideal Pt_3Mn structure featuring 8 Pt−Pt bonds and 4 Pt−Mn bonds for each Pt atom (the actual coordination numbers are lower due to coordination-unsaturated NP surface). The results for the Pt_3Mn-s catalyst (7.4 Pt−Pt at 2.72 Å and 1.4 Pt−Mn at 2.70 Å) are characteristic of a mixture of Pt and Pt_3Mn phases, with a coordination number ratio of Pt−Pt to Pt−Mn around 5. X-

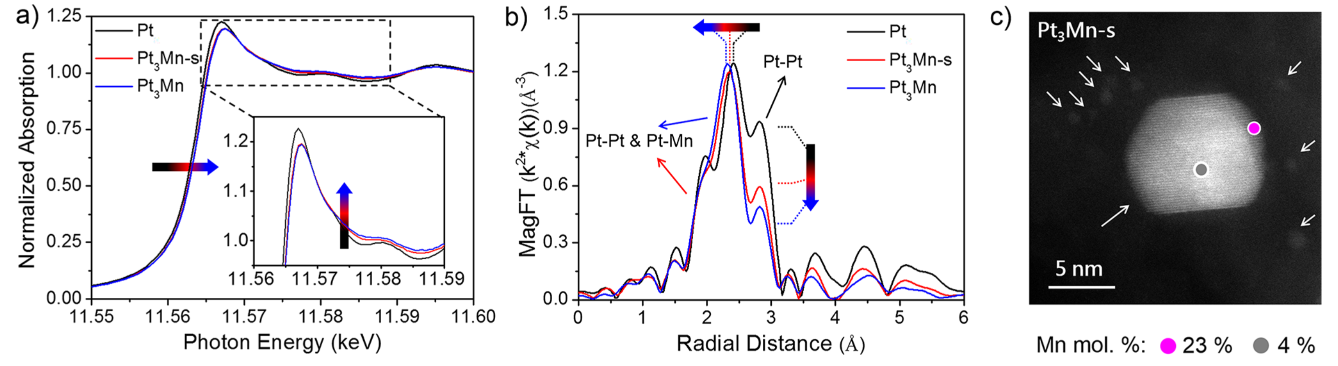

Figure 2. a) Pt L_{III} edge XANES of the reduced catalysts; b) magnitude of Fourier Transform of the k^2 weighted EXAFS spectra of the reduced catalysts, Δk = 3.0−12.2 Å; c) local Mn concentration along the side surface of the NP vs down the NP top surface through the whole diameter for the Pt_3Mn-s sample with core−shell structure measured by EDS on one of the few larger-than-average NPs.

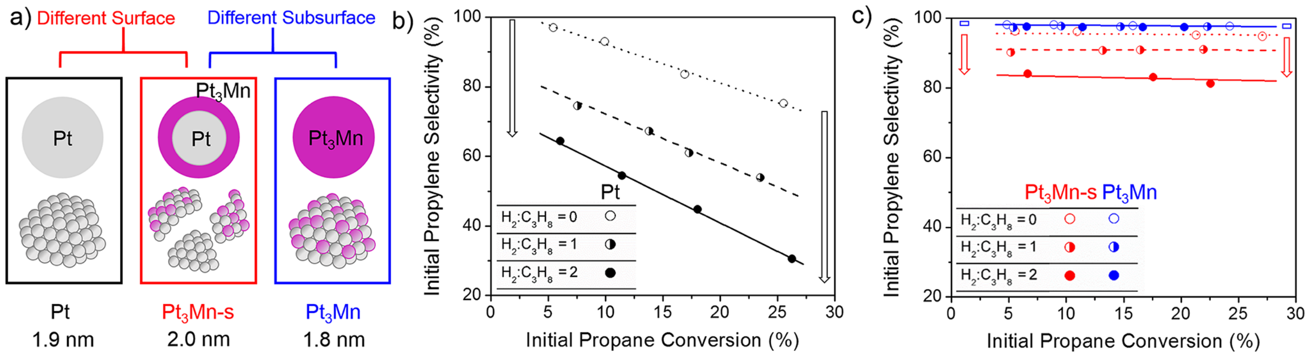

Figure 3. a) A schematic view of the structure of the three catalysts and b) propane dehydrogenation selectivity vs conversion at 550 °C for Pt and c) for Pt_3Mn-s and Pt_3Mn under a different H_2:C_3H_8 molar ratio in the feed (H_2/C_3H_8) of 0 (hollow circle and dotted line), 1 (half-filled circle and dashed line), and 2 (filled circle and solid line). The three different lines overlap for Pt_3Mn.

ray photoelectron spectroscopy (XPS) of the samples reduced in a spectrometer side chamber and not exposed to air also supports Pt−Mn intermetallic compound formation according to higher binding energy in the Pt 4f region and Mn^0 in the Mn 2p region (Figure S3). The excess Mn in the catalysts stayed oxidized and highly dispersed according to XAS, XPS (Figure S3, Figure S4, Table S3), and sXRD.

To discern whether the Pt and Pt_3Mn phases in the Pt_3Mn-s catalyst do form a core−shell geometry or stay simply as a physical mixture of the two, the surface composition of the catalysts is investigated by taking the EXAFS difference (Figure S5c) of the reduced (Figure 2b) versus air exposed samples (Figure S5b). Upon air exposure, the NP surface is oxidized, and the numbers of Pt-Metal bonds decrease (note that the Pt_3Mn phase contains Pt−Pt and Pt−Mn bonds).[32,33] Such changes can be isolated in the difference XAS spectra and are reflective of the surface composition. The fitting result shows that for Pt_3Mn-s, the loss of surface metal−metal bonds includes both Pt−Pt and Pt−Mn paths (Table S4). The ratio between the number of Pt−Pt and Pt−Mn bonds is around 2, much smaller than the value obtained for the whole nanoparticle average (around 5), suggesting that the Mn concentration is much higher on the surface and that Pt_3Mn-s catalyst is not a physical mixture of the Pt and Pt_3Mn phases. More importantly, this surface coordination number ratio of 2 is the same as that of the ideal Pt_3Mn intermetallic structure as well as the value obtained from the difference XAS of the Pt_3Mn catalyst. Therefore, the surface of the Pt_3Mn-s catalyst has the Pt_3Mn intermetallic structure. The monometallic Pt phase is present in the NP core. Formation of similar core−shell structures has been recently reported for NPs with other compositions prepared in the same way.[25,27] Energy-dispersive X-ray spectroscopy (EDS, Figure S6) collected on the Pt_3Mn-s catalyst further verified the core−shell structure. Point scans on one of the few larger-than-average NP generated enough counts (Figure 2c). The molar percentage of Mn detected near the side surface of the NP (the magenta dot) was 23%, very close to the theoretical Mn concentration on a Pt_3Mn phase, and much higher than that of the location through the diameter across the core region (4%, gray dot), confirming that the Pt_3Mn phase located on and near the NP surface while Pt localized in the core.

Together, detailed structural characterizations establish that two different intermetallic Pt−Mn NP catalysts with different subsurfaces have been made (Figure 3a). The Pt_3Mn catalyst contains uniform intermetallic NPs with Pt_3Mn structure on both the surface and subsurface, while Pt_3Mn-s has core−shell NPs with an ordered Pt_3Mn intermetallic surface on a Pt core. Comparing these two catalysts allows for evaluation of the effect of different subsurface (Pt vs Pt_3Mn) on the catalytic performance of supported NPs with the same Pt_3Mn surface. This subsurface effect can also be distinguished from a classic surface effect shown by the difference between Pt_3Mn-s and the reference Pt catalyst.

Olefin (C−H Activation Product) Selectivity during Propane Dehydrogenation. The effect of NP subsurface composition on selectivity of C−H over C−C bond activation was evaluated by a model reaction propane dehydrogenation (PDH) at 550 °C for the two Pt−Mn catalysts together with the reference Pt NP catalyst.[34] The selectivity to propylene (the product of C−H activation) was compared under the same propane concentrations but varying cofed hydrogen concentrations. The effect of the surface composition is observed from comparison of Pt_3Mn-s and Pt. Figure 3b shows that the selectivity of the Pt catalyst drops from 95% to 78% as the conversion increases in the absence of cofed hydrogen and further to ∼35% as the H_2 to C_3H_8 molar ratio (H_2/C_3H_8) increases from 0 to 2. This is due to substantial activity for the side reaction hydrogenolysis, which breaks C−C bonds with the assistance of hydrogen, and is consistent with previous reports.[35] In contrast, for the Pt_3Mn-s catalyst (Figure 3c), the C−H selectivity remains nearly constant with the PDH conversion, which is consistent with the absence of Pt phase on the core−shell NP surface. As the H_2/C_3H_8 increases from 0 to 2, the selectivity decreases from 95% to 82%, which is a much smaller change compared to Pt.

Comparing Pt_3Mn to Pt_3Mn-s discloses a distinct subsurface effect that is independent from the surface structure. As shown in Figure 3c, the selectivity of Pt_3Mn remains high at 98% not only under varying conversion similar to Pt_3Mn-s but also under increasing H_2 to C_3H_8 molar ratio. Increasing H_2/C_3H_8 from 0 to 2, which significantly lowers the selectivity of Pt_3Mn-s as well as Pt, has little effect on Pt_3Mn. The hydrogenolysis side reaction is almost completely suppressed on Pt_3Mn. This implies that the interaction of Pt_3Mn with the reactants and intermediates is significantly altered by the subsurface composition.

The assignment of the promoted catalytic performance to different subsurface structures is strengthened by the observation that the Pt−Mn catalysts maintain their structures under reaction condition. *In situ* sXRD under propane dehydrogenation atmosphere at 550 °C and even 750 °C

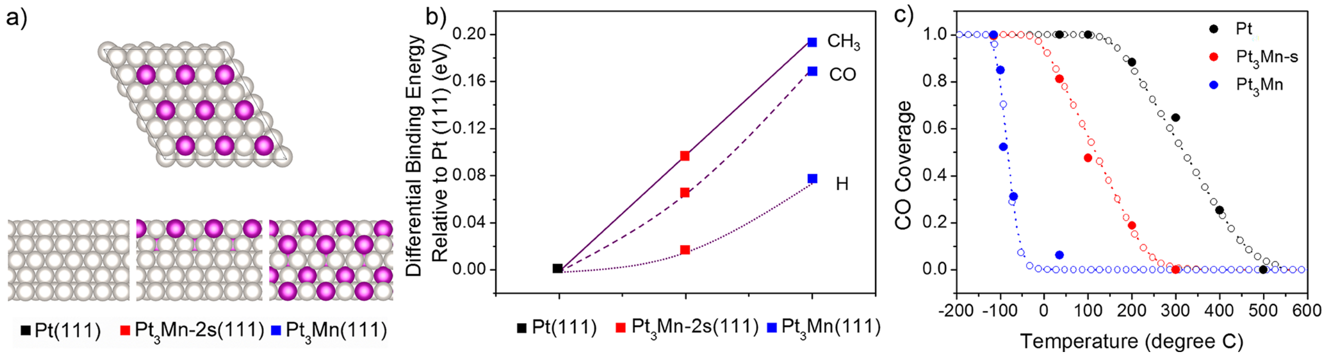

Figure 4. a) The structure model for a Pt_3Mn (111) top surface and the side view of the models used for DFT calculation of binding energies on Pt (Pt(111)), Pt_3Mn-s (Pt_3Mn-2s(111), 2 layers of Pt_3Mn on top of Pt), and Pt_3Mn (Pt_3Mn-(111)); b) the calculated differential binding energy of H, CO, and CH_3 on the (111) surface of Pt, Pt_3Mn-s, and Pt_3Mn; c) CO chemisorption surface coverage vs temperature for Pt, Pt_3Mn-s, and Pt_3Mn. The filled circles are experimental data, while the hollow circles and dotted lines are from the best fit to the Temkin model.

recorded identical patterns including the superlattice features and peak widths (Figure S7, except for thermal lattice expansion) compared to the reduced catalysts at room temperature and 550 °C, suggesting that the Pt_3Mn surface and/or subsurface on the NPs remained ordered during high temperature reaction. Not only the Pt_3Mn intermetallic catalyst but also the core−shell NPs in the Pt_3Mn-s catalyst are stable during high temperature reaction due to limited solid state diffusion of Mn. After initial reduction of Mn and its subsequent diffusion into the Pt lattice, the oxidized Mn concentration near the NPs decreases, turning off further reduction by hydrogen spillover. Therefore, a structural evolution of the Pt−Mn catalysts is not observed, and the NP structure is determined by the initial Mn concentration on the support surface. The stable catalyst structure in part contributes to long-term stable catalytic performance. While Pt quickly deactivates with time on-stream, both Pt−Mn catalysts do not. They show stable conversion for PDH at 550 °C for at least a week (until the test was terminated, Figure S8) with turnover rates in the 0.1 to 1 s^{-1} range as expected for Pt catalysts according to the literature.[34,36,37] STEM imaging on the spent catalysts after PDH for 1 week shows size distributions similar to those of the fresh catalysts (Figure S9), indicating minimal particle sintering. The Pt_3Mn catalyst was also evaluated for dehydrogenation of ethane, which requires higher reaction temperature. For 25% ethane balanced in N_2 at 750 °C, the Pt_3Mn catalyst shows stable performance with >90% selectivity at around 40% conversion for at least 1 day (Figure S8), demonstrating the high temperature stability of this intermetallic phase during catalytic reaction.

Subsurface Electronic Effect on Surface Adsorption. To better understand the observed subsurface effect on the catalytic performance, DFT calculations were undertaken on models (Figure 4a) representing the three catalyst structures. A Pt_3Mn full-body intermetallic was considered for the Pt_3Mn sample. A Pt_3Mn shell on top of Pt with single or double layers of Pt_3Mn was considered for Pt_3Mn-s. This catalyst was expected to have between one or two outer Pt_3Mn layers on 2 nm core−shell NPs, since the molar percentage of the Pt_3Mn intermetallic shell out of the whole NP was estimated to be between ∼40−60% according to the average lattice parameter measured by sXRD and the coordination number ratio of Pt-Mn/Pt-Pt from EXAFS fits. The models were compared with monometallic Pt. The (111) facet was chosen based on its low surface free energy for both pure Pt and Pt_3Mn. The binding energies for hydrogen (H) and the methyl group (CH_3, as a model chemisorbed hydrocarbon species) were calculated, since the improvement in selectivity for light alkane dehydrogenation has been previously suggested to correlate with the altered adsorption strength of the catalyst to hydrocarbon molecules and hydrogen.[38,39] The binding energy of carbon monoxide (CO) was also calculated as well as measured experimentally. The computational results are summarized in Figure 4b. Compared to Pt, two layers of a Pt_3Mn shell (Pt_3Mn-2s(111)) reduce the binding energy by 0.02, 0.07, and 0.09 eV for H, CO, and CH_3, respectively, whereas binding energies are reduced by 0.08, 0.17, and 0.19 eV for H, CO, and CH_3 on the full Pt_3Mn intermetallic surface. Importantly, the Pt_3Mn full-body intermetallic has a weaker adsorption energy for all investigated adsorbates as compared to the Pt_3Mn intermetallic shell on Pt subsurface, confirming the presence of the subsurface effect. The results are consistent with the promotion of PDH selectivity of Pt_3Mn compared to Pt_3Mn-s, since the weaker adsorption is correlated with the preferential desorption of hydrocarbon and hydrogen species over their participation in the steps leading to C−C bond breaking side reaction hydrogenolysis.[39,40]

The changes in catalyst adsorption capability due to subsurface effect is also evident from experimental measurements of equilibrium CO adsorption on the supported NPs, giving heats of adsorption on different catalysts. As seen in Figure 4c, all three catalysts show one-step CO desorption, including Pt_3Mn-s, again consistent with this catalyst having a single surface composition characteristic of core−shell structure rather than a physical mixture of Pt and Pt_3Mn. For Pt, CO chemisorption is saturated at room temperature.[41] In contrast, saturation uptake for Pt_3Mn-s is not achieved until around 0 °C, whereas for Pt_3Mn it is only observed below −120 °C. Fitting the coverage-temperature data to the Temkin model (see the SI),[42,43] the heats of adsorption of CO on Pt at 0 and full coverage ($\Delta H(0)$ and $\Delta H(1)$) are estimated to be $\Delta H(0)$ = 130 kJ/mol and $\Delta H(1)$ = 70 kJ/mol, close to literature results and giving an average heats of adsorption ΔH_{ave} = 100 kJ/mol.[41] For Pt_3Mn-s, the best fit Temkin desorption curve results in $\Delta H(0)$ = 85 kJ/mol, $\Delta H(1)$ = 40 kJ/mol, and ΔH_{ave} = 63 kJ/mol, and for Pt_3Mn, the best fit Temkin desorption curve results in $\Delta H(0)$ = 30 kJ/mol, $\Delta H(1)$ = 25 kJ/mol, and ΔH_{ave} = 28 kJ/mol, respectively. The average heat of adsorption is lowered by 37 kJ/mol comparing Pt_3Mn-s to Pt. Similarly, the average heats of adsorption of

Pt_3Mn is 35 kJ/mol lower than Pt_3Mn-s. These experimental results on the NP catalysts are consistent with the trends seen in the DFT calculations and correlate well with the increasing propane dehydrogenation selectivity for Pt_3Mn-s and Pt_3Mn. The changes in the reduction of heats of CO adsorption are higher than the DFT predictions,[39,40,44,45] which is likely related to adsorption on corners and edges on the NPs. We note that adsorption of CO on a model high index surface, such as the (211) step, shows the same trend between different catalysts but with a larger reduction in binding energy due to subsurface Pt_3Mn as compared to the (111) terrace (Table S4).

Additional DFT calculations were conducted on varying model structures. Constraining the lattice constant of the Pt_3Mn shell to values between pure Pt_3Mn and Pt only changes binding energies by less than 30 meV (Table S4), suggesting the absence of a major surface strain effect, which is also expected from the very similar lattice parameters between the Pt_3Mn and the Pt phases. In addition, a single layer Pt_3Mn shell on Pt does not reduce the binding energy significantly as compared to pure Pt (Table S5). Therefore, Mn in the subsurface plays a key role in reducing the surface adsorption strength, most likely through bonding of subsurface atoms with the catalytic surface. This is consistent with previous DFT studies on model structures containing other elements.[6,7] According to the *d* band theory, an electronic effect leading to weaker adsorption strength is typically related with downward shifts of *d* states away from the Fermi level,[46] which is indeed observed from the calculated density of states, showing a −0.05 eV shift for Pt_3Mn (111) compared to Pt_3Mn-2s(111) (Figure S10). This shift of the overall *d* states usually leads to lower average energy of the occupied *d* states but is also accompanied by a small upward shift of the average energy of the unoccupied Pt 5*d* states. The latter is observed on our Pt−Mn catalysts in the increase in the energy of the Pt L_{III} edge by *in situ* XANES (Figure 2a). Such shifts of occupied and unoccupied *d* states were recently measured for a similar Pt_1Zn_1 intermetallic NP catalyst by *in situ* Resonant Inelastic X-ray Scattering (RIXS).[47] The shifts are similar to typical changes of the HOMO and LUMO orbitals in a molecule upon bonding interactions and are likely results of the strong heterometal bonding interaction of the intermetallic compounds.[47] This study suggests that such intermetallic interaction can be manipulated by a diffusion controlled solid state transformation starting from the NP surface to the core for tuning the subsurface structure of NPs. Such controlled intermetallic formations have been demonstrated for several intermetallic compositions and are possible for many other phases, both on noble metal NP cores as well as intermetallic cores.[25−27] The resulting subsurface effect modifies the adsorptive properties of the surface sites to offer enhanced catalytic performance.

■ CONCLUSION

Supported NP catalysts with different subsurface composition were prepared by controlled intermetallic formation and confirmed by *in situ* characterization under reaction conditions at high temperature, allowing for evaluation of the influence of subsurface composition to the adsorptive and catalytic properties. With the same ordered NP surface, a Pt_3Mn intermetallic subsurface instead of monometallic Pt significantly improved the C−H activation selectivity during propane dehydrogenation by lowering the heats of hydrocarbon and hydrogen adsorption of the surface sites. Models presented herein provide a beginning to microkinetic modeling to help in directly identifying the driving force for selectivity differences. This work highlights the distinct role of subsurface layers for altering the surface chemical and catalytic properties on NP catalysts. Such a subsurface effect can be tuned via controlled synthesis of NPs with atomically precise intermetallic phases, promising a wide composition range for versatile catalyst design targeting different catalytic processes.[14]

■ ASSOCIATED CONTENT

Ⓢ Supporting Information

The Supporting Information is available free of charge on the ACS Publications website at DOI: 10.1021/jacs.8b08162.

> Experimental details, HAADF STEM images of fresh and spent catalysts, detailed EXAFS fitting results, XPS spectra, XANES spectra of Mn references, EDS spectra, XRD patterns, light alkane dehydrogenation conversion vs time, and DFT binding energies (PDF)

■ AUTHOR INFORMATION

Corresponding Authors

*gzhang@dlut.edu.cn (G.Z.)
*mill1194@purdue.edu (J.T.M.)

ORCID

Tao Ma: 0000-0002-0579-8045
Yue Wu: 0000-0002-9820-2000
Jeffrey Greeley: 0000-0001-8469-1715
Guanghui Zhang: 0000-0002-5854-6909
Jeffrey T. Miller: 0000-0002-6269-0620

Present Address

State Key Laboratory of Fine Chemicals, PSU-DUT Joint Center for Energy Research, School of Chemical Engineering, Dalian University of Technology (G.Z.) and Department of Chemical Engineering, Stanford University (Z.W.).

Notes

The authors declare no competing financial interest.

■ ACKNOWLEDGMENTS

This paper is based upon work supported in part by the National Science Foundation under Cooperative Agreement No. EEC-1647722. Z.W. and J.T.M. gratefully acknowledge the financial support provided by Davidson School of Chemical Engineering, Purdue University and use of the Electron Microscopy Facility at Birck Nanotechnology Center, Purdue University. The XPS data was obtained at the Surface Analysis Facility of the Birck Nanotechnology Center of Purdue University. Use of the Advanced Photon Source was supported by the U.S. Department of Energy, Office of Basic Energy Sciences, under contract no. DE-AC02-06CH11357. MRCAT operations, beamline 10-BM, are supported by the Department of Energy and the MRCAT member institutions. The authors also acknowledge the use of beamline 11-ID-C at APS.

■ REFERENCES

(1) Bond, G. C. Supported metal catalysts: some unsolved problems. *Chem. Soc. Rev.* **1991**, *20*, 441−475.

(2) Chorkendorff, I.; Niemantsverdriet, J. W. *Concepts of modern catalysis and kinetics*; John Wiley & Sons: 2006.

(3) Sinfelt, J. H. Catalysis by alloys and bimetallic clusters. *Acc. Chem. Res.* **1977**, *10*, 15−20.
(4) Campbell, R. A.; Rodriguez, J. A.; Goodman, D. W. Chemical and electronic properties of ultrathin metal films: the Pd/Re (0001) and Pd/Ru (0001) systems. *Phys. Rev. B: Condens. Matter Mater. Phys.* **1992**, *46*, 7077.
(5) Chen, J. G.; Menning, C. A.; Zellner, M. B. Monolayer bimetallic surfaces: Experimental and theoretical studies of trends in electronic and chemical properties. *Surf. Sci. Rep.* **2008**, *63*, 201−254.
(6) Greeley, J.; Mavrikakis, M. Alloy catalysts designed from first principles. *Nat. Mater.* **2004**, *3*, 810.
(7) Stephens, I. E.; Bondarenko, A. S.; Perez-Alonso, F. J.; Calle-Vallejo, F.; Bech, L.; Johansson, T. P.; Jepsen, A. K.; Frydendal, R.; Knudsen, B. P.; Rossmeisl, J. Tuning the activity of Pt(111) for oxygen electroreduction by subsurface alloying. *J. Am. Chem. Soc.* **2011**, *133*, 5485−5491.
(8) Escudero-Escribano, M.; Malacrida, P.; Hansen, M. H.; Vej-Hansen, U. G.; Velázquez-Palenzuela, A.; Tripkovic, V.; Schiøtz, J.; Rossmeisl, J.; Stephens, I. E.; Chorkendorff, I. Tuning the activity of Pt alloy electrocatalysts by means of the lanthanide contraction. *Science* **2016**, *352*, 73−76.
(9) Kim, D.; Xie, C.; Becknell, N.; Yu, Y.; Karamad, M.; Chan, K.; Crumlin, E. J.; Nørskov, J. K.; Yang, P. Electrochemical Activation of CO_2 through Atomic Ordering Transformations of AuCu Nanoparticles. *J. Am. Chem. Soc.* **2017**, *139*, 8329−8336.
(10) Alayoglu, S.; Nilekar, A. U.; Mavrikakis, M.; Eichhorn, B. Ru−Pt core−shell nanoparticles for preferential oxidation of carbon monoxide in hydrogen. *Nat. Mater.* **2008**, *7*, 333.
(11) Nilekar, A. U.; Alayoglu, S.; Eichhorn, B.; Mavrikakis, M. Preferential CO oxidation in hydrogen: reactivity of core− shell nanoparticles. *J. Am. Chem. Soc.* **2010**, *132*, 7418−7428.
(12) Tao, F.; Grass, M. E.; Zhang, Y.; Butcher, D. R.; Renzas, J. R.; Liu, Z.; Chung, J. Y.; Mun, B. S.; Salmeron, M.; Somorjai, G. A. Reaction-driven restructuring of Rh-Pd and Pt-Pd core-shell nanoparticles. *Science* **2008**, *322*, 932−934.
(13) Armbrüster, M.; Schlögl, R.; Grin, Y. Intermetallic compounds in heterogeneous catalysis—a quickly developing field. *Sci. Technol. Adv. Mater.* **2014**, *15*, 034803.
(14) Furukawa, S.; Komatsu, T. Intermetallic compounds: promising inorganic materials for well-structured and electronically modified reaction environments for efficient catalysis. *ACS Catal.* **2017**, *7*, 735−765.
(15) Ferro, R.; Saccone, A. *Intermetallic chemistry*; Elsevier: 2008.
(16) Vej-Hansen, U. G.; Rossmeisl, J.; Stephens, I. E.; Schiøtz, J. Correlation between diffusion barriers and alloying energy in binary alloys. *Phys. Chem. Chem. Phys.* **2016**, *18*, 3302−3307.
(17) Gallagher, J. R.; Childers, D. J.; Zhao, H.; Winans, R. E.; Meyer, R. J.; Miller, J. T. Structural evolution of an intermetallic Pd-Zn catalyst selective for propane dehydrogenation. *Phys. Chem. Chem. Phys.* **2015**, *17*, 28144−28153.
(18) Kresse, G.; Furthmüller, J. Efficiency of ab-initio total energy calculations for metals and semiconductors using a plane-wave basis set. *Comput. Mater. Sci.* **1996**, *6*, 15−50.
(19) Kresse, G.; Furthmüller, J. Efficient iterative schemes for ab initio total-energy calculations using a plane-wave basis set. *Phys. Rev. B: Condens. Matter Mater. Phys.* **1996**, *54*, 11169.
(20) Kresse, G.; Hafner, J. Ab initio molecular dynamics for liquid metals. *Phys. Rev. B: Condens. Matter Mater. Phys.* **1993**, *47*, 558.
(21) Kresse, G.; Hafner, J. Ab initio molecular-dynamics simulation of the liquid-metal−amorphous-semiconductor transition in germanium. *Phys. Rev. B: Condens. Matter Mater. Phys.* **1994**, *49*, 14251.
(22) Perdew, J. P.; Burke, K.; Ernzerhof, M. Generalized gradient approximation made simple. *Phys. Rev. Lett.* **1996**, *77*, 3865.
(23) Blöchl, P. E. Projector augmented-wave method. *Phys. Rev. B: Condens. Matter Mater. Phys.* **1994**, *50*, 17953.
(24) Kresse, G.; Joubert, D. From ultrasoft pseudopotentials to the projector augmented-wave method. *Phys. Rev. B: Condens. Matter Mater. Phys.* **1999**, *59*, 1758.
(25) Wu, Z.; Wegener, E. C.; Tseng, H.-T.; Gallagher, J. R.; Harris, J. W.; Diaz, R. E.; Ren, Y.; Ribeiro, F. H.; Miller, J. T. Pd−In intermetallic alloy nanoparticles: highly selective ethane dehydrogenation catalysts. *Catal. Sci. Technol.* **2016**, *6*, 6965−6976.
(26) Wegener, E. C.; Wu, Z.; Tseng, H.-T.; Gallagher, J. R.; Ren, Y.; Diaz, R. E.; Ribeiro, F. H.; Miller, J. T. Structure and reactivity of Pt−In intermetallic alloy nanoparticles: Highly selective catalysts for ethane dehydrogenation. *Catal. Today* **2018**, *299*, 146−153.
(27) Childers, D. J.; Schweitzer, N. M.; Shahari, S. M. K.; Rioux, R. M.; Miller, J. T.; Meyer, R. J. Modifying structure-sensitive reactions by addition of Zn to Pd. *J. Catal.* **2014**, *318*, 75−84.
(28) Wu, L.; Fournier, A.; Willis, J. J.; Cargnello, M.; Tassone, C. J. In Situ X-ray Scattering Guides the Synthesis of Uniform PtSn Nanocrystals. *Nano Lett.* **2018**, *18*, 4053.
(29) Ye, C.; Wu, Z.; Liu, W.; Ren, Y.; Zhang, G.; Miller, J. T. Structure Determination of a Surface Tetragonal Pt_1Sb_1 Phase on Pt Nanoparticles. *Chem. Mater.* **2018**, *30*, 4503−4507.
(30) Regalbuto, J. *Catalyst preparation: science and engineering*; CRC Press: 2016.
(31) Williams, D.; Jezierski, A. Magnetic order in crystallographically ordered Pt4-y (MnxCr1-x) y alloys. *J. Magn. Magn. Mater.* **1986**, *59*, 41−56.
(32) Gallagher, J. R.; Li, T.; Zhao, H.; Liu, J.; Lei, Y.; Zhang, X.; Ren, Y.; Elam, J. W.; Meyer, R. J.; Winans, R. E. In situ diffraction of highly dispersed supported platinum nanoparticles. *Catal. Sci. Technol.* **2014**, *4*, 3053−3063.
(33) Miller, J. T.; Schreier, M.; Kropf, A. J.; Regalbuto, J. R. A fundamental study of platinum tetraammine impregnation of silica: 2. The effect of method of preparation, loading, and calcination temperature on (reduced) particle size. *J. Catal.* **2004**, *225*, 203−212.
(34) Sattler, J. J.; Ruiz-Martinez, J.; Santillan-Jimenez, E.; Weckhuysen, B. M. Catalytic dehydrogenation of light alkanes on metals and metal oxides. *Chem. Rev.* **2014**, *114*, 10613−10653.
(35) Galvita, V.; Siddiqi, G.; Sun, P.; Bell, A. T. Ethane dehydrogenation on Pt/Mg(Al)O and PtSn/Mg(Al)O catalysts. *J. Catal.* **2010**, *271*, 209−219.
(36) Siddiqi, G.; Sun, P.; Galvita, V.; Bell, A. T. Catalyst performance of novel Pt/Mg (Ga)(Al) O catalysts for alkane dehydrogenation. *J. Catal.* **2010**, *274*, 200−206.
(37) Sun, P.; Siddiqi, G.; Vining, W. C.; Chi, M.; Bell, A. T. Novel Pt/Mg (In)(Al)O catalysts for ethane and propane dehydrogenation. *J. Catal.* **2011**, *282*, 165−174.
(38) Nykänen, L.; Honkala, K. Selectivity in Propene Dehydrogenation on Pt and Pt3Sn Surfaces from First Principles. *ACS Catal.* **2013**, *3*, 3026−3030.
(39) Yang, M.-L.; Zhu, Y.-A.; Zhou, X.-G.; Sui, Z.-J.; Chen, D. First-principles calculations of propane dehydrogenation over PtSn catalysts. *ACS Catal.* **2012**, *2*, 1247−1258.
(40) Nykänen, L.; Honkala, K. Density functional theory study on propane and propene adsorption on Pt (111) and PtSn alloy surfaces. *J. Phys. Chem. C* **2011**, *115*, 9578−9586.
(41) Bourane, A.; Dulaurent, O.; Bianchi, D. Heats of adsorption of linear and multibound adsorbed CO species on a Pt/Al_2O_3 catalyst using in situ infrared spectroscopy under adsorption equilibrium. *J. Catal.* **2000**, *196*, 115−125.
(42) Temkin, M.; Pyzhev, V. Kinetics of ammonia synthesis on promoted iron catalysts. *Acta Physiochim. URSS* **1940**, *12*, 217−222.
(43) Bourane, A.; Bianchi, D. Heats of adsorption of the linear CO species on Pt/Al_2O_3 using infrared spectroscopy: impact of the Pt dispersion. *J. Catal.* **2003**, *218*, 447−452.
(44) Cortright, R.; Dumesic, J. Microcalorimetric, spectroscopic, and kinetic studies of silica supported Pt and Pt/Sn catalysts for isobutane dehydrogenation. *J. Catal.* **1994**, *148*, 771−778.
(45) Shen, J.; Hill, J. M.; Watwe, R. M.; Spiewak, B. E.; Dumesic, J. A. Microcalorimetric, Infrared Spectroscopic, and DFT Studies of Ethylene Adsorption on Pt/SiO_2 and $Pt-Sn/SiO_2$ Catalysts. *J. Phys. Chem. B* **1999**, *103*, 3923−3934.
(46) Hammer, B.; Nørskov, J. K. Theoretical surface science and catalysis—calculations and concepts. *Adv. Catal.* **2000**, *45*, 71−129.

(47) Cybulskis, V. J.; Bukowski, B. C.; Tseng, H.-T.; Gallagher, J. R.; Wu, Z.; Wegener, E.; Kropf, A. J.; Ravel, B.; Ribeiro, F. H.; Greeley, J. Zinc Promotion of Platinum for Catalytic Light Alkane Dehydrogenation: Insights into Geometric and Electronic Effects. *ACS Catal.* **2017**, *7*, 4173−4181.